Bifunctional GeC/SnSSe heterostructure for high-efficient photocatalyst and photovoltaic devices

Xinxin Jiang,[a] Wenli Xie,[a] Xuhui Xu,[a] Quan Gao,[a] Dongmei Li,[*a] Bin Cui,[*a] Desheng Liu,[*a] and Fanyao Qu[b]

[a]*School of Physics, State Key Laboratory of Crystal Materials, Shandong University, Jinan 250100, China.*

[b] *Instituto de F ́ısica, Universidade de Bras ́ılia, Bras ́ılia-DF 70919-970, Brazil.*

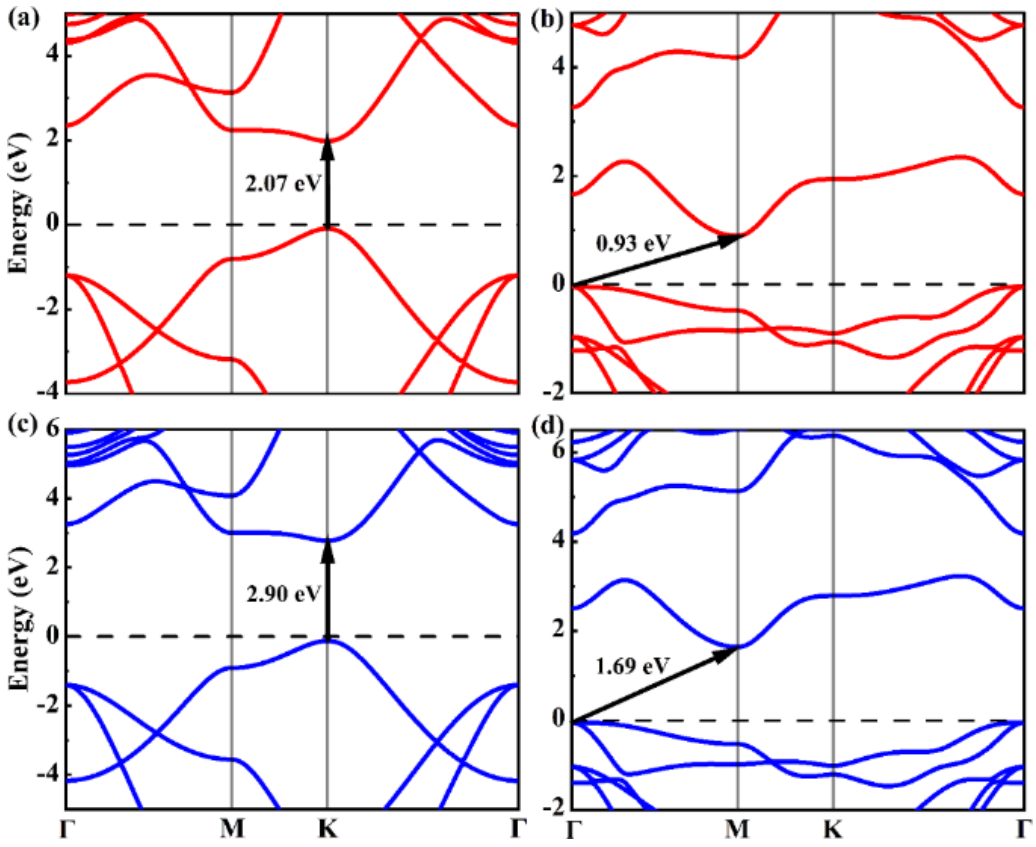

Fig. S1 Calculated electronic bandstructures for (a) GeC and (b) SnSSe monolayers at the PBE functional (solid red line) as well as (c) GeC and (d) SnSSe monolayers at HSE06 functional (solid blue line). The black arrows indicate the bandgap. The Fermi level is set as zero.

* *Corresponding author. Email:* li_dm@sdu.edu.cn (D.M. Li); cuibin@sdu.edu.cn (B. Cui); liuds@sdu.edu.cn (D.S. Liu).

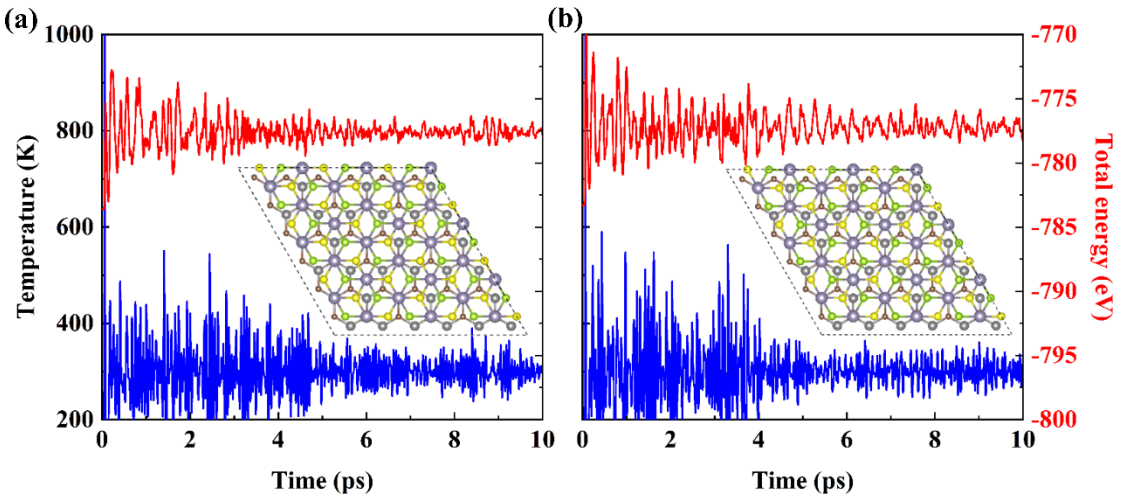

Fig. S2 Temporal evolution of temperature (blue line) and total energy (red line) of (a) GeC/SeSnS and (b) GeC/SSnSe vdWHs during AIMD simulations for 10 ps at 300 K. Insets: The final structural configurations after 10 ps at 300K.

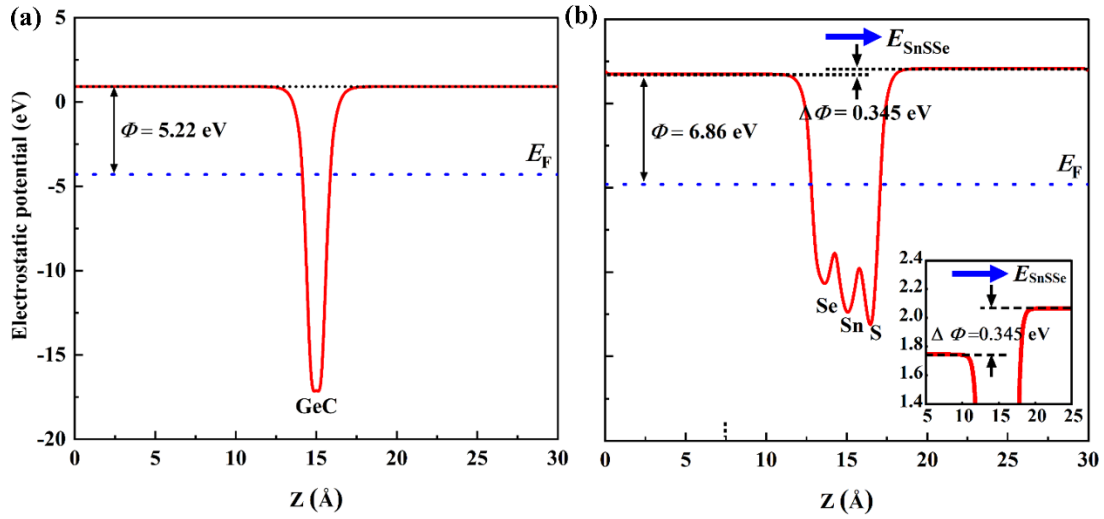

Fig. S3 Calculated electrostatic potential along the *z*-direction for the (a) GeC and (b) SnSSe monolayers, respectively. The black and blue dotted lines denote the vacuum energy and Fermi energy level, respectively. Inset: the zoom-in view of the electrostatic potential around 15 Å for SnSSe monolayer.

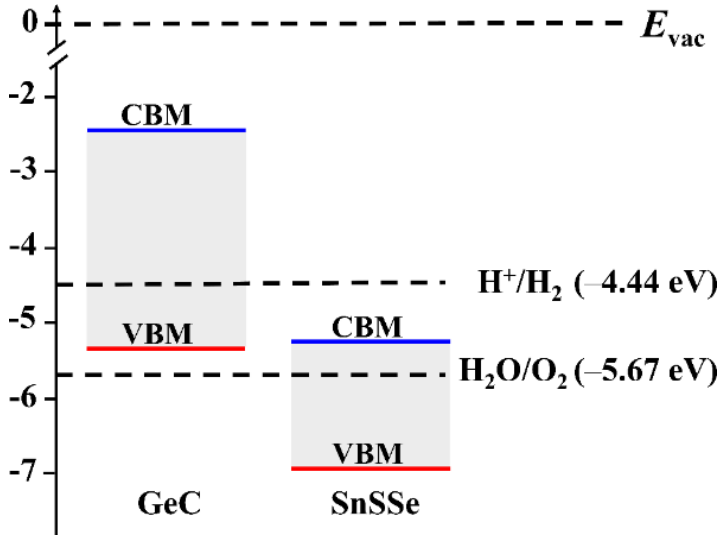

Fig. S4 Band edge positions of the isolated GeC and SnSSe monolayers referring to the vacuum level obtained by the HSE06 level.

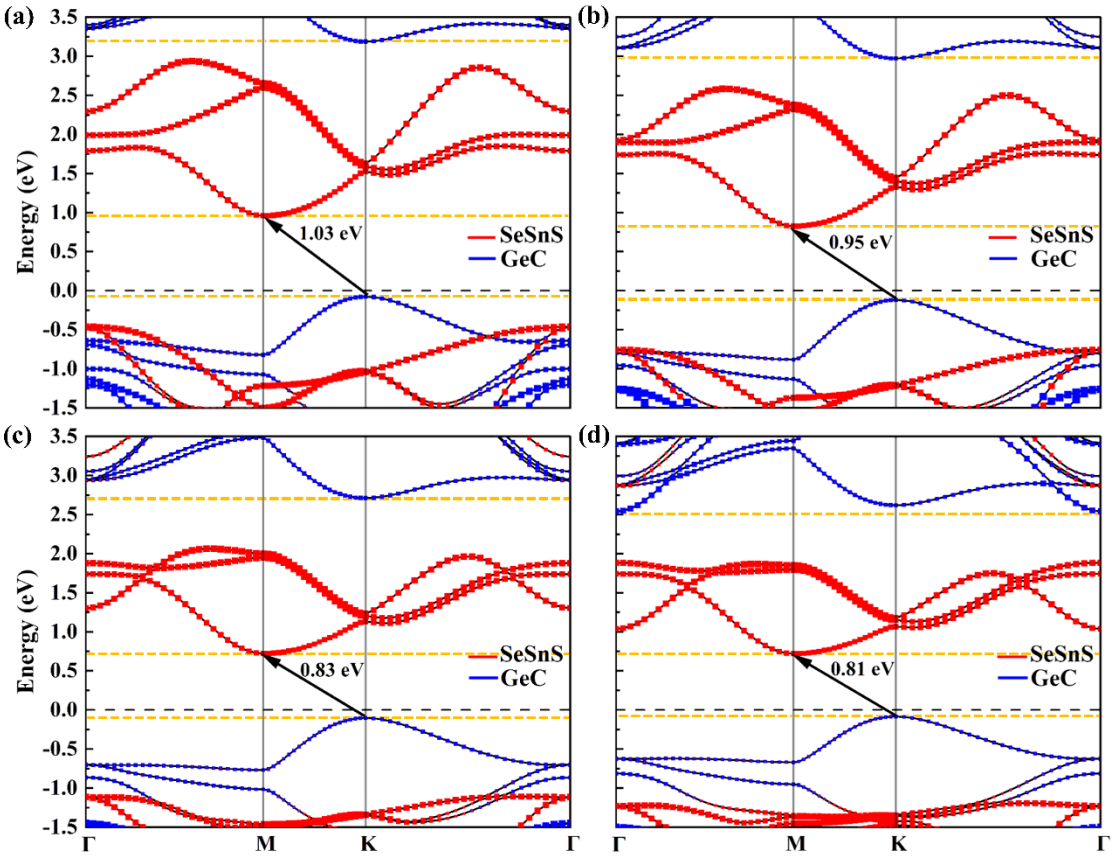

Fig. S5 Projected electronic bandstructures of GeC/SeSnS vdWH under different biaxial strains, (a) –4%, (b) –2%, (c) 2%, and (d) 4%, respectively, obtained by HSE06 level. The red and blue curves correspond to the bands from SnSSe and GeC layers, respectively. The black arrows indicate the bandgap. The dashed orange horizontal lines as a guide to the eye indicate the band edges.

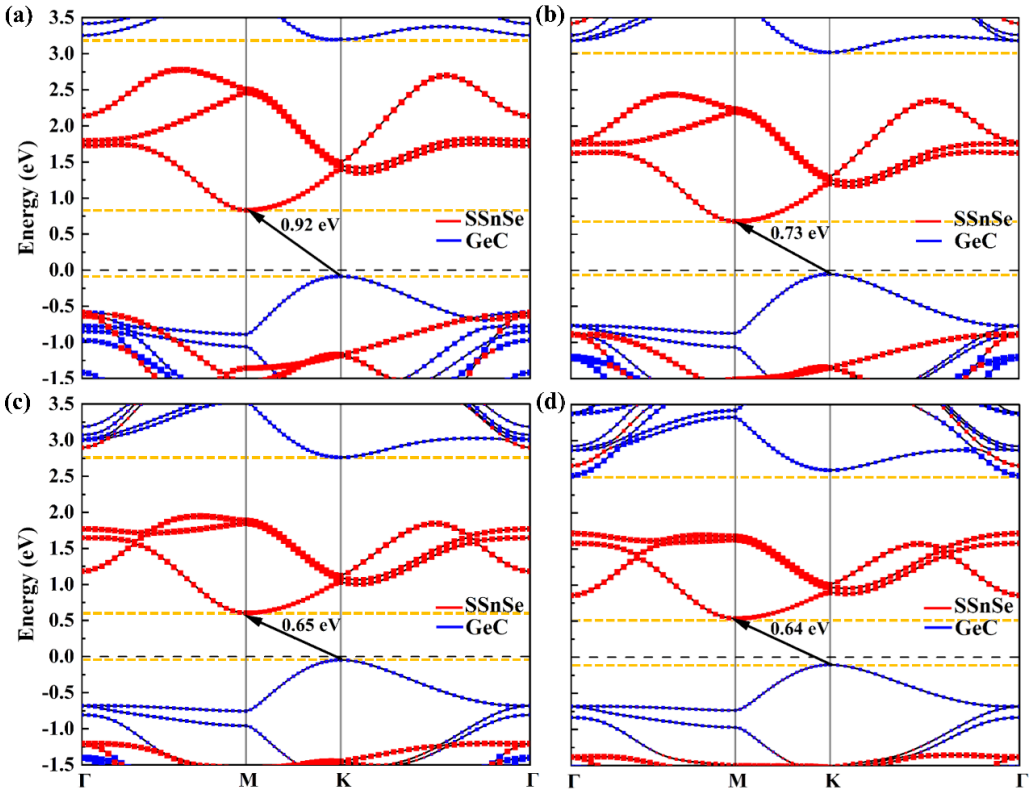

Fig. S6 Projected electronic bandstructures of GeC/SSnSe vdWH under different biaxial strains, (a) –4%, (b) –2%, (c) 2%, and (d) 4%, respectively, obtained by HSE06 level. The red and blue curves correspond to the bands from SnSSe and GeC layers, respectively. The black arrows indicate the bandgap. The dashed orange horizontal lines as a guide to the eye indicate the band edges.

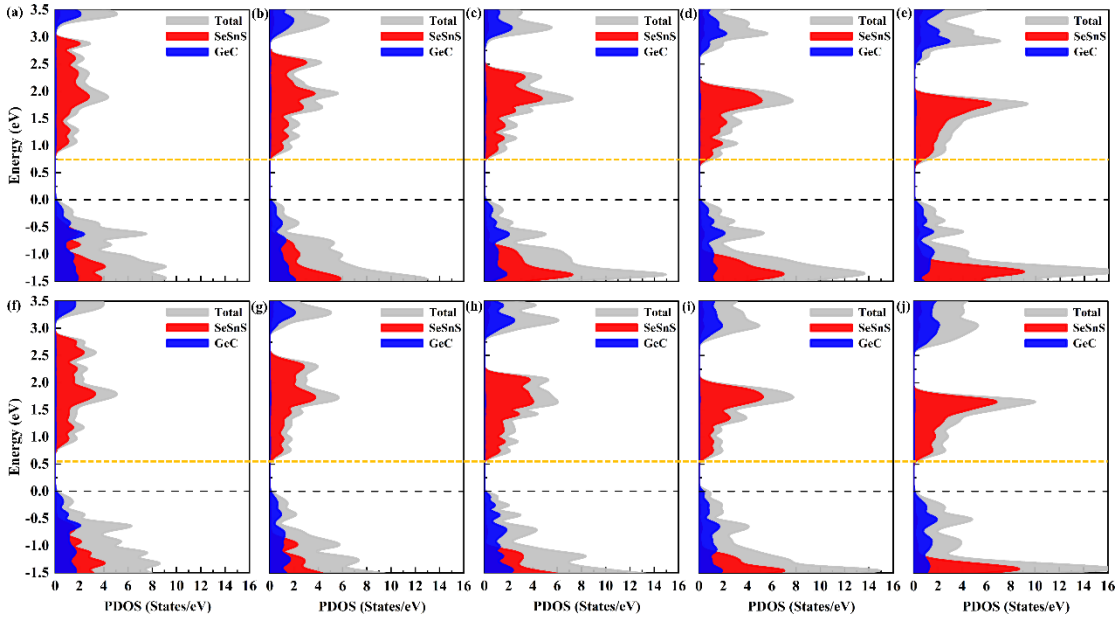

Fig. S7 Projected density of states of GeC/SnSSe vdWHs under different biaxial strains, (a) –4%, (b) –2%, (c) 0%, (d) 2%, and (e) 4% for GeC/SeSnS vdWH, respectively. (f, g, h, i, and j) are the same as (a, b, c, d, and e), but for GeC/SSnSe vdWH. The results are obtained by HSE06 level. The dashed orange horizontal lines as a guide to the eye indicate the band edge of intrinsic GeC/SnSSe vdWHs.

To confirm the reliability of our calculations, we performed similar calculations on similar but more studied vdWHs such as MoS_2/WS_2 using the same computational method. Firstly, we calculated the crystal and electronic structures of the MoS_2 and WS_2 monolayers. According to the bandstructure of MoS_2 and WS_2, as shown in Fig. S8(a) and (b), we can see that both monolayers are semiconductors with direct bandgaps of 2.22 and 2.38 eV, respectively. The projected bandstructure of the MoS_2/WS_2 vdWH is shown in Fig. S8(c), as obtained from HSE06 calculations. One can see that the MoS_2/WS_2 vdWH preserves the characteristic of the semiconductor with a global indirect bandgap of 1.89 eV. The blue and red marks in the projected bandstructure represent the contribution from the MoS_2 and WS_2 monolayers, respectively, which means the conduction band minimum (CBM) and the valence band maximum (VBM) of the MoS_2/WS_2 vdWH originate from MoS_2 and WS_2 monolayers, respectively, forming a type-II band alignment, as shown in Fig. S8(d). The spatial separation of the CBM and VBM facilitates the suppression of the recombination probability of photogenerated electrons and holes and promotes the separating of the photogenerated electron–hole pairs. Interestingly, the related experiments were also reported in MoS_2/WS_2 vdWH. Hill *et al*. synthesized the MoS_2/WS_2 heterostructure using mechanical exfoliation and transfer techniques. They found a type-II band alignment by analyzing the tunneling spectra for each monolayer constituent and their heterostructure region.[1] The PL intensity of the MoS_2/WS_2 heterostructure decreased by half compared to the single MoS_2 or WS_2 materials, indicating the more effective separation of the photogenerated electron–hole phenomenon due to the type-II band alignment.[2] Through combined photoluminescence spectroscopy and optical pump–probe spectroscopy, Hong *et al*. demonstrated that an ultrafast charge transfer took place very efficiently in MoS_2/WS_2 heterostructures. In particular, holes in the MoS_2 layer can separate into the WS_2 layer within 50 fs upon photoexcitation, further demonstrating the type-II band alignment.[3]

Moreover, the photogenerated electrons lying in the CBs of MoS_2 can proceed HER. Meanwhile, the photogenerated holes residing in the WS_2 layer can realize the OER. The calculated STH efficiencies of the MoS_2 and WS_2 monolayers, and

MoS_2/WS_2 vdWH are 12.58%, 9.55%, and 21.16%, respectively, as shown in Table S1, indicating that the construction of MoS_2/WS_2 vdWH can enhance the solar-to-hydrogen efficiency higher than that of the single MoS_2 monolayer about 70%. This result is consistent with the experimental observations by Shi *et al*. They synthesized MoS_2/WS_2 heterostructure by using a growth-temperature-mediated two-step chemical vapor deposition strategy for photocatalytic applications, and found that relative enhancements (the H_2 evolution rate of MoS_2/WS_2 is about 1.819 μmol cm^{-2} h^{-1}, while that of MoS_2 is about 1.003 μmol cm^{-2} h^{-1}) in photocatalytic activities of MoS_2/WS_2 under illumination, because the type-II band alignment enables directional electron flow from electrode to the active site.[4]

We also calculated the photocurrent densities in MoS_2 and WS_2 monolayers, and MoS_2/WS_2 vdWH illuminated by a linearly polarized light with a power of 16 $\mu W \cdot mm^{-2}$ as a function of photon energy. Compared with the MoS_2 and WS_2 monolayers, the photocurrent of the MoS_2/WS_2 vdWH is significantly enhanced, as shown in Fig. S9. The total photocurrent densities are obtained from the current at each photon energy weighted by the flux of the AM1.5G standard solar spectrum. The calculated (J_{ph}) are up to 14.86, 15.35, and 134.38 $\mu A \cdot mm^{-2}$ for MoS_2 and WS_2 monolayers, and MoS_2/WS_2 vdWH-based devices, respectively. The overall photocurrent of the vdWH is nearly 10 times higher than those of the monolayers. Similar results were experimentally obtained by Pesci *et al*.[5] They reported that the MoS_2/WS_2 heterojunction exhibits incident-photon-to-current-efficiencies (IPCE) 10 times greater than those of films comprised of the individual constituents, and the photocurrent generated by the heterojunction is 1 order of magnitude larger.

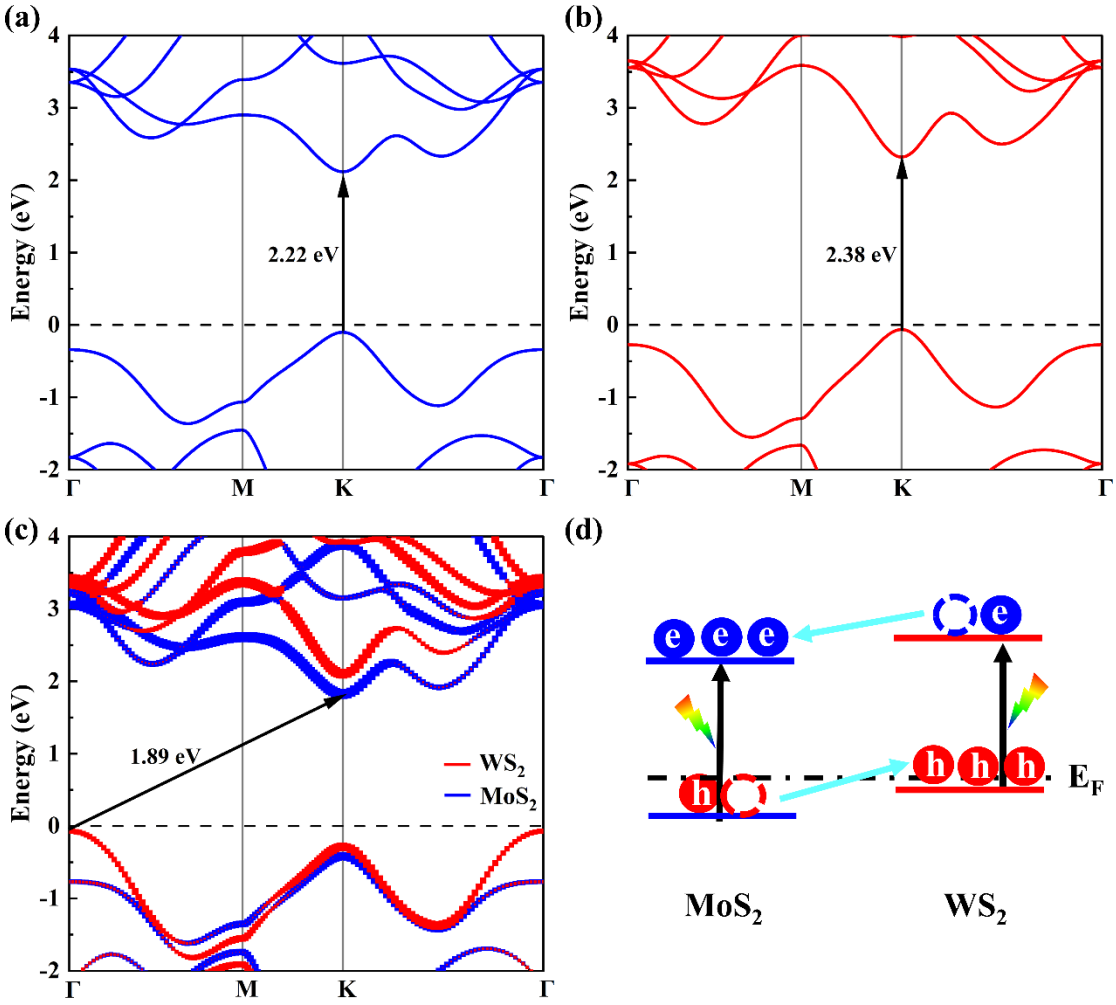

Fig. S8 Calculated electronic bandstructures for (a) MoS_2 and (b) WS_2 monolayers at HSE06 functional, respectively. (c) Projected electronic bandstructures for the MoS_2/WS_2 vdWH at HSE06 level. (d) Type-II band alignment of the MoS_2/WS_2 vdWH.

Table S1 Energy conversion efficiency of optical absorption (η_{abs}), carrier utilization (η_{cu}), STH (η_{STH}), and corrected STH (η'_{STH}) for the MoS_2 and WS_2 monolayers, and MoS_2/WS_2 vdWH.

	η_{abs} (%)	η_{cu} (%)	η_{STH} (%)
MoS_2	27.43	45.88	12.58
WS_2	21.75	43.90	9.55
MoS_2/WS_2	41.68	50.76	21.16

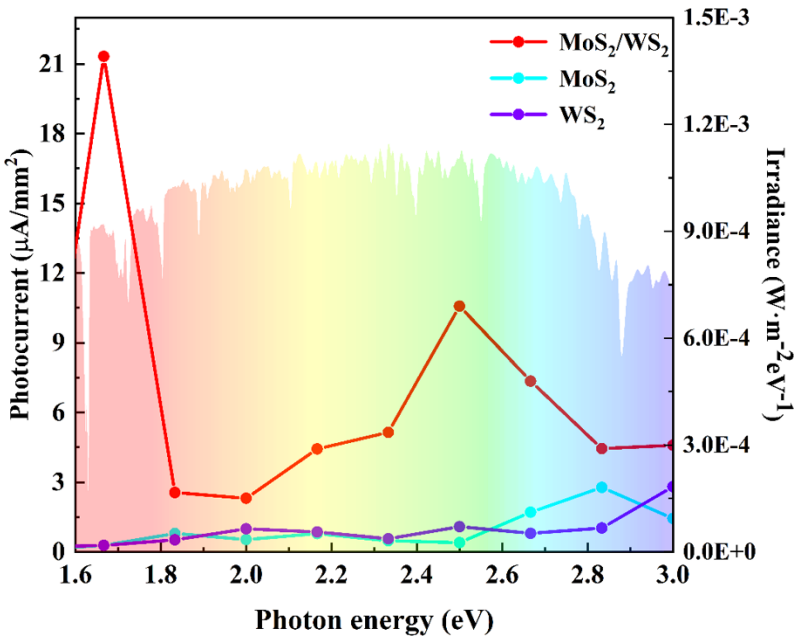

Fig. S9 Photocurrent densities in MoS_2 and WS_2 monolayers, and MoS_2/WS_2 vdWH illuminated by a linearly polarized light with a power of 16 $\mu W \cdot mm^{-2}$ as a function of photon energy.

References

1 H. M. Hill, A. F. Rigosi, K. T. Rim, G. W. Flynn and T. F. Heinz, *Nano Lett.*, 2016, **16**, 4831–4837.

2 T. Han, H. Liu, S. Wang, S. Chen and K. Yang, *Molecules*, 2020, **25**, 1857.

3 X. Hong, J. Kim, S. F. Shi, Y. Zhang, C. Jin, Y. Sun, S. Tongay, J. Wu, Y. Zhang and F. Wang, *Nat. Nanotechnol.*, 2014, **9**, 682–686.

4 J. Shi, R. Tong, X. Zhou, Y. Gong, Z. Zhang, Q. Ji, Y. Zhang, Q. Fang, L. Gu, X. Wang, Z. Liu and Y. Zhang, *Adv. Mater.*, 2016, **28**, 10664–10672.

5 F. M. Pesci, M. S. Sokolikova, C. Grotta, P. C. Sherrell, F. Reale, K. Sharda, N. Ni, P. Palczynski and C. Mattevi, *ACS Catal.*, 2017, **7**, 4990–4998.